

# A simple vortex model of a thunderstorm downburst – a parametric evaluation

Jesson, Michael; Sterling, Mark

DOI:

[10.1016/j.jweia.2017.12.001](https://doi.org/10.1016/j.jweia.2017.12.001)

License:

Creative Commons: Attribution-NonCommercial-NoDerivs (CC BY-NC-ND)

*Document Version*

Peer reviewed version

*Citation for published version (Harvard):*

Jesson, M & Sterling, M 2018, 'A simple vortex model of a thunderstorm downburst – a parametric evaluation', *Journal of Wind Engineering and Industrial Aerodynamics*, vol. 174, pp. 1-9.  
<https://doi.org/10.1016/j.jweia.2017.12.001>

[Link to publication on Research at Birmingham portal](#)

## General rights

Unless a licence is specified above, all rights (including copyright and moral rights) in this document are retained by the authors and/or the copyright holders. The express permission of the copyright holder must be obtained for any use of this material other than for purposes permitted by law.

- Users may freely distribute the URL that is used to identify this publication.
- Users may download and/or print one copy of the publication from the University of Birmingham research portal for the purpose of private study or non-commercial research.
- User may use extracts from the document in line with the concept of 'fair dealing' under the Copyright, Designs and Patents Act 1988 (?)
- Users may not further distribute the material nor use it for the purposes of commercial gain.

Where a licence is displayed above, please note the terms and conditions of the licence govern your use of this document.

When citing, please reference the published version.

## Take down policy

While the University of Birmingham exercises care and attention in making items available there are rare occasions when an item has been uploaded in error or has been deemed to be commercially or otherwise sensitive.

If you believe that this is the case for this document, please contact [UBIRA@lists.bham.ac.uk](mailto:UBIRA@lists.bham.ac.uk) providing details and we will remove access to the work immediately and investigate.

# A simple vortex model of a thunderstorm downburst – a parametric evaluation

Mike Jesson and Mark Sterling

*University of Birmingham, Edgbaston, Birmingham, UK*

ABSTRACT: Thunderstorm downbursts are short-lived, transient extreme wind events which can cause wind speeds equivalent to a category EF3 tornado (~150mph). The complex flow field which they produce has previously been the subject of time-expensive numerical modelling. However, it is well-known that there is a large, random variation in full-scale downbursts and so a quick, easily varied model would be of benefit to engineers calculating dynamic loading on structures. This paper introduces a simple and computationally inexpensive vortex model of a downburst, which is shown to model the main features of the flow field in a physically simulated thunderstorm downburst to an appropriate degree of accuracy.

KEYWORDS: Transient winds, numerical model, vortex, thunderstorm, downburst.

## 1 INTRODUCTION

A thunderstorm downburst is a transient, highly localised extreme wind event which can cause wind speeds of 150mph, equivalent to a category EF3 tornado ([1]). These events are created by the cooling of (and precipitation within) warm, moist, rising air in a convective thunderstorm cell, which then reverses direction to form a downdraft which impinges on the ground. A primary ring vortex forms around the downdraft, and is carried radially outwards with the outflow from the impingement point. The superposition of the outflow and vortex flow fields creates a region of very high wind speed. Numerical simulations also indicate the development of a smaller, secondary vortex at the base of the primary ([2], [3]), caused by the interaction of the flow and ground roughness. The combination of these flow elements results in a flow field which is very different from that seen in atmospheric boundary layer (ABL) flows. Unlike ABL winds, which for the purposes of design are regarded as statistically stationary over a number of hours and uniform over tens of kilometres, downbursts typically have a lifetime of only a few minutes and a downdraft radius of approximately 1 – 2km, with a non-stationary time-series. The vertical distribution of radial wind-speed typically has a peak maximum ( $u_m$ , the spatio-temporal maximum over the whole flow field) close to the ground, at a height ( $z_m$ ) of 30 – 100m at full-scale. These features are illustrated for the physically simulated downburst which is the subject of this paper in Figure 1. One feature of downbursts is the variability of such events, with no two recorded downbursts producing precisely the same flow fields ([4]–[6]), although there are clear similarities between the large-scale characteristics.

There is growing consensus that severe thunderstorm events may become more frequent due to climate change (e.g. [7]). Consequently, efforts have been made to understand the wind

38 loading which they exert. Due to the difficulty in predicting where and when a downburst will  
 39 occur, along with the usual issues of variability, the use of full-scale measurements for the  
 40 determination of downburst wind loading is problematic (though the work of Lombardo ([5])  
 41 provides a very useful data set for validation). For this reason, simulations are used to model  
 42 downbursts and (in some cases) their effects on structures, both physically (e.g. [8]–[13]) and  
 43 numerically ([3], [14], [15]). The more advanced physical simulators, such as that used by  
 44 McConville et al. ([16]) and Jesson et al. ([11], [12]), model the transient nature of a downburst  
 45 event, and exhibit the same run-to-run variation which has been seen as with full-scale events  
 46 ([16]). This variation limits the insight which can be gained, although general loading patterns  
 47 may be quantified (e.g. [11], [12]). On the numerical side, techniques such as Large Eddy  
 48 Simulation and cloud models have been used, with the lifecycle of the downburst being  
 49 simulated from the initial downdraft to the formation and motion of the ring vortex. Although  
 50 they are of importance in elucidating the mechanisms which drive a downburst and lead to their  
 51 high wind speeds, these techniques are computational expensive. Holmes and Oliver [17]  
 52 suggested a simple empirical model, based around a time-varying impinging jet profile.  
 53 Arguably, this model lacks a clear relationship to the components making up the complex flow  
 54 field, and therefore does not suitably model vertical variation.

55

56

57

58

59

60

61

62

63

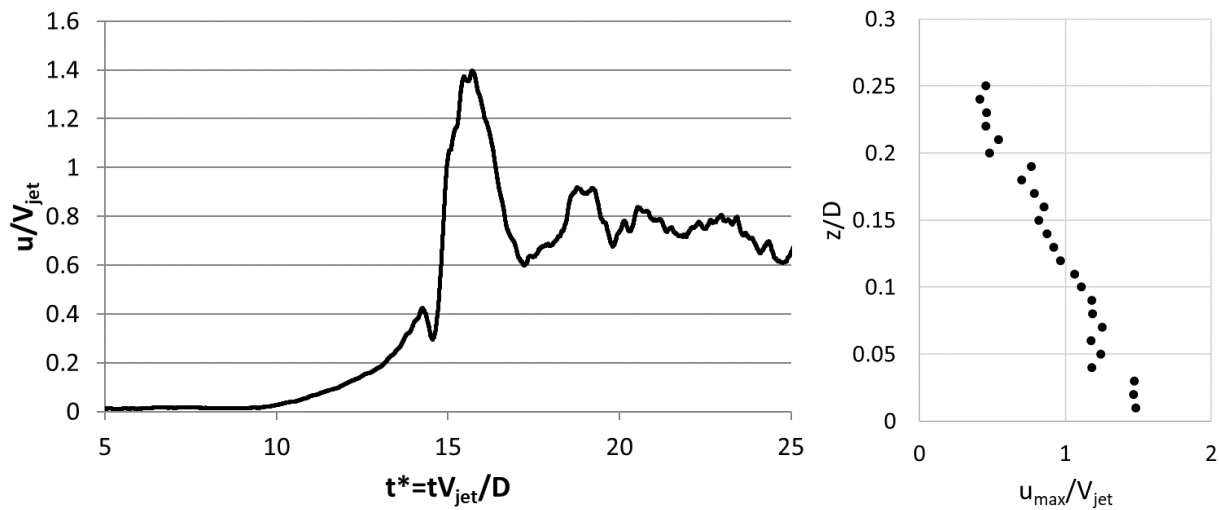
64

65

66

67

68



69

70

71

**Figure 1: (left) Wind-speed time-series and (right) vertical profile of temporal maximum wind speeds from a physically simulated downburst**

72 A simple numerical model of a downburst is presented in this paper. This model extends the  
73 concepts developed for the purpose of flight simulation by Ivan ([18]) and Schultz ([19]), who  
74 developed potential flow models of stationary, time-invariant downburst flows. Before  
75 presenting the model definition, a brief description of the University of Birmingham Transient  
76 Wind Simulator (UoB-TWS) is given in Section 2; experimental data from the UoB-TWS  
77 provides the reference data for model validation. The model, which is described fully in Section  
78 3, calculates the velocity field as a superposition of a primary vortex, secondary vortex and linear  
79 outflow velocity. Section 4 compares model output with the UoB-TWS data, and includes a  
80 parametric study which identifies the important parameters in defining and creating a downburst  
81 flow field. Finally, important conclusions from this work are presented.

## 82 2 UNIVERSITY OF BIRMINGHAM TRANSIENT WIND SIMULATOR (UOB-TWS)

83 The UoB-TWS is a vertical impinging jet downburst simulator with a length scale estimated  
84 as 1:1600 and is described fully by Jesson et al. ([11], [12]). Aperture control is used to simulate  
85 the rapid flow accelerations which occur in full-scale downbursts and the simulator has been  
86 shown to simulate the transient aspects of a downburst flow ([11], [12], [16]). Run-to-run  
87 variation is seen in the simulations, as has been noted in full-scale events and mentioned in the  
88 introduction. In order to investigate the generic aspects of downbursts, while minimising the  
89 effects of such variation, an ensemble-mean approach has been used in analysing the UoB-TWS  
90 data. Thus, time-series from multiple runs are averaged according to:

$$u(t) = \frac{1}{N} \sum_{n=1}^N u_n(t) \quad (1)$$

91 where  $u(t)$  is the ensemble-mean velocity time-series,  $n$  is the run index,  $N$  is the total  
92 number of runs in the ensemble and  $u_n(t)$  is the velocity time-series from the  $n^{th}$   
93 experimental run. Ensemble-mean values are used in this paper.

94 The aim of the original UoB experiments was to measure the wind loading on building  
95 models in a simulated downburst. The velocity measurements had two purposes: Firstly, to  
96 identify the position,  $(x_m, z_m)$ , of the peak maximum outflow velocity (found to be  $x_m/D =$   
97  $1.50$ ,  $z_m/D = 0.02$ ), where  $x$  is the radial distance from the centre of the downdraft,  $z$  is the  
98 vertical position and  $D$  is the diameter of the simulated downdraft and  $m$  denotes a maximum),  
99 and secondly to ensure that the vertical profile of radial velocity at this point was consistent with  
100 full-scale data (which was demonstrated by comparison with the work of Hjelmfelt ([20]; see  
101 [12])). Velocity measurements were made at 10mm vertical spacings for profiles measured at  
102  $x/D = 1.00$ ,  $1.50$ ,  $2.00$  and  $2.50$ , with partial profiles (vertical positions around  $z_m$  only) at  
103  $x/D = 1.25$  and  $1.75$  to verify that the  $x/D = 1.50$  profile included the maximum velocity  
104 point.

106 3.1 *Model Development*

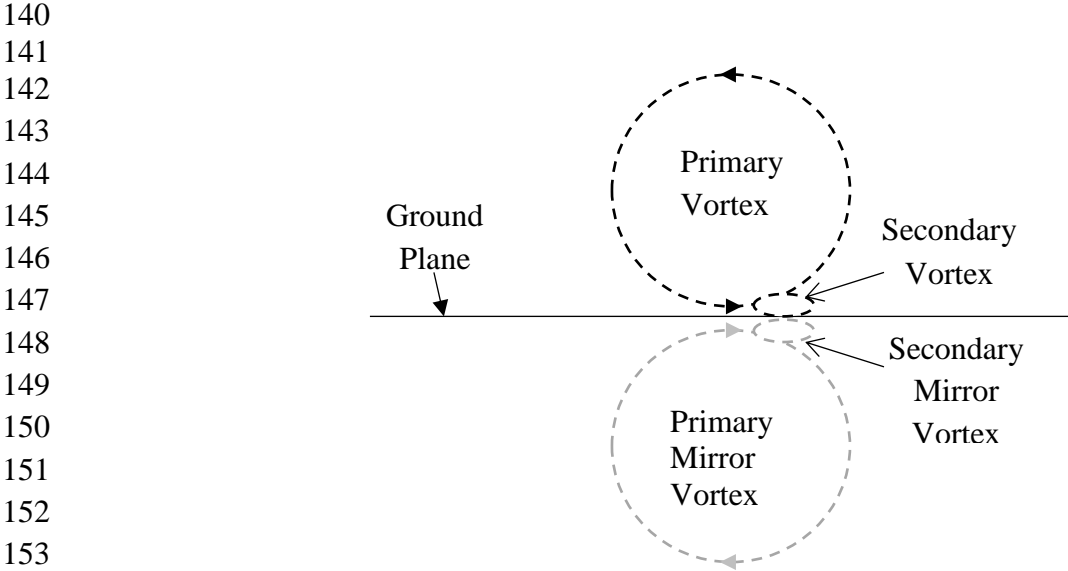
107 An early version of the vortex model has been presented by Jesson and Sterling ([21]) and this  
 108 description is expanded and updated here. This model uses similar concepts to those applied by  
 109 Ivan ([18]) and Schultz ([19]), with the addition of a secondary vortex component and temporal  
 110 variation. A non-translating downburst is simulated, i.e., the downburst is not part of a larger  
 111 storm which carries the downburst with it (although incorporating the translation of the storm  
 112 would be programmatically straightforward as an improved understanding of the movement of a  
 113 downburst front within the wider storm becomes available). This permits the assumption that the  
 114 downdraft creates an axially symmetric outflow around the impingement point, meaning that  
 115 model is 2-D within a cylindrical polar coordinate system; variation occurs along the radial ( $x$ )  
 116 and vertical ( $z$ ) directions only. The respective velocities are  $u$  and  $w$ , and the velocity field is  
 117 assumed to be the superposition of three, independent velocity fields, one from each of the main  
 118 flow structures:

- 119 • The main outflow from the downdraft impingement point.
- 120 • The primary ring vortex.
- 121 • The secondary vortex.

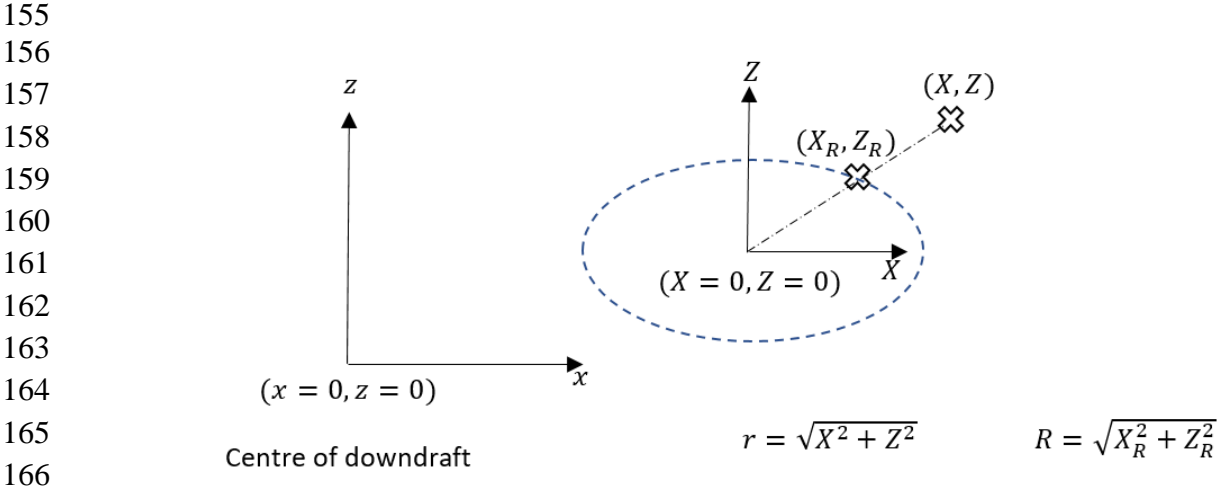
122 This superposition is a technique applied in (inviscid) potential flow models, as is the use of  
 123 mirrored vortices (Figure 2) to ensure that the condition of zero flow across the ground plane is  
 124 met. The mirroring of the vortices also accelerates the radial flow close to the boundary, as  
 125 required by continuity to reflect the contraction of the flow field by the ground plane. The  
 126 inviscid model also means that there is no “no-slip” condition at the ground plane; however, at  
 127 present the variation of velocity very close to the ground (i.e., the boundary layer) remains an  
 128 open point. Thus, vertical velocity profiles and been plotted for the above ground region ( $z/D >$   
 129  $0.01$ ). Radial motion of the vortices is governed purely by the outflow velocity (a model  
 130 parameter; vertical motion is a separate model parameter, as discussed later). This outflow  
 131 velocity is modelled as linearly increasing (more details are given in Section 3.2). In standard  
 132 potential flow theory, the flow is assumed to be inviscid, leading to vortices with a singularity at  
 133 the centre. In this model, each vortex is an independent (viscous) Rankine-type vortex. For a  
 134 circular Rankine vortex with a core of radius  $R$  and circulation  $\Gamma$ , the tangential wind speed at a  
 135 radial distance  $r$  from the centre,  $V_\theta(r)$ , is given by:

$$V_\theta(r) = \begin{cases} \frac{\Gamma r}{2\pi R^2} = \frac{\Gamma\sqrt{X^2 + Z^2}}{2\pi(X_R^2 + Z_R^2)} \text{ for } r \leq R \\ \frac{\Gamma}{2\pi r} = \frac{\Gamma}{2\pi\sqrt{X^2 + Z^2}} \text{ for } r > R \end{cases} \quad (2)$$

137 where, in the Cartesian form,  $(X, Z)$  is a general point in the domain,  $(X_R, Z_R)$  lies on the core  
 138 boundary, and capitals indicate a local coordinate system with its origin at the vortex centre  
 139 (Figure 3).



154 **Figure 2: Schematic application of mirrored vortices.**



167 **Figure 3: Definition of the coordinate system.**

168  
 169 In order to estimate the relative positions and speeds of the three elements of the flow field,  
 170 reference was made to rudimentary flow visualisation work at the University of Birmingham  
 171 ([16], [22]) and the numerical work of Mason ([3]) and Kim & Hangan ([2]). From these it was  
 172 observed that:

- 173 • The primary vortex changes shape (becoming elliptical) and weakens (reducing circulation)  
 174 with time, i.e. as it spreads out from the centre of the impingement zone. In addition to the  
 175 reduction in circulation, it also lifts from the ground.

- 176 • The secondary vortex is initially not present, but strengthens with time before weakening. It  
 177 forms at the leading edge of the primary vortex, at ground level but, according to Mason’s  
 178 CFD simulations, ([3]) is lifted by the rotation of the primary vortex.

179 The vortex model outlined in this paper, includes parameters to govern the initial size, shape,  
 180 position and strength of each vortex, and also the rate of change of these parameters. For the  
 181 secondary vortex, a “half-life” can be configured, such that the magnitude of the vortex increases  
 182 up to the half-life, following which the vortex weakens. The full list of parameters is given in  
 183 Table 1.

184 The evolution of the vortices from circular to elliptical has been incorporated in the model  
 185 through specifying the rate of change of the length of the ellipse axes, one of which is parallel to  
 186 the  $x$ -axis and the other parallel to the  $z$ -axis. The circumference of the vortex core is thus  
 187 defined by:

$$\frac{X_R^2}{a(t)^2} + \frac{Z_R^2}{b(t)^2} = 1 \quad (3)$$

188 where  $a(t)$  and  $b(t)$  are the lengths of the principal axes, which vary with time,  $t$ .  $V_\theta(r)$   
 189 is then calculated using a modified version of (2) such that  $r$  is the distance along the line  
 190 joining the centre of the ellipse and the point at which the velocity is calculated, and  $R$  is the  
 191 ellipse radius along that line (Figure 3).

192

193 **Table 1 Vortex model parameters.**

Parameter	“Best Fit”		Estimate from UoB Data
	Primary Vortex	Secondary Vortex	
Initial circulation ( $m^2/s$ )	18.00	0.00	20.00
Rate of change of circulation ( $m^2/s^2$ )	-35.00	-7.00	
Initial $x, z$ radii ( $m$ )	0.30, 0.30 <sup>a</sup>	0.08, 0.005 <sup>c</sup>	0.4, 0.4
Rate of change of $x, z$ radii ( $m/s$ )	0.10, -0.02 <sup>c&amp;e</sup>	0.00, 0.02 <sup>c&amp;e</sup>	
Initial centre position, $x, z$ ( $m$ )	0.80 <sup>b</sup> , 0.30 <sup>b</sup>	0.88 <sup>d</sup> , 0.005 <sup>e</sup>	
Translation speed, $x, z$ -directions ( $m/s$ )	Varies <sup>f</sup> , 0.00	Varies <sup>g</sup> , Varies <sup>e</sup>	
Half-life ( $s$ )	N/A	0.20	
Final Outflow Velocity ( $m/s$ )	10.00		
Time Step ( $s$ )	0.01		
Grid Spacing* ( $m$ )	0.25		

194

195

196

\*Grid spacing does not affect the values calculated for each grid node.  
 Superscript letters indicate parameters which, for the determination of the Best Fit, are calculated from other parameters according to the referenced assumption(s) detailed in Section 3.2.

197 3.2 *Parameter Quantification*

198 Values for the model parameters were initially estimated from the references stated above,  
199 and then refined to improve the fit of the model to the UoB-TWS data while ensuring that the  
200 values remained representative of the reference data. The refinement process involved  
201 incrementing model parameters over multiple runs and then identifying the “best fit”  
202 configuration. In order to make the number of runs manageable (by reducing the number of  
203 varied parameters and hence parameter combinations) it was assumed that:

- 204 a) The primary vortex is initially circular.
- 205 b) The primary vortex always starts with its bottom edge touching the ground plane and its rear  
206 edge touching the edge of the downdraft region (i.e., the initial position is a function of the  
207 initial size, and does not vary independently; the vortex “edge” is at radius  $R$ ).
- 208 c) The combination of the rate of change of  $z$ -radius and  $z$ -translation speed is such that  $R =$   
209  $0.02m = z_m$  when the secondary vortex has its greatest circulation.
- 210 d) The secondary vortex starts with its rear edge at the centreline of the primary vortex.
- 211 e) At its vertical centre, the secondary vortex spans the distance between the ground plane and  
212 the primary vortex.
- 213 f) The translation speed is the outflow speed. This is initially zero, but increases to the final  
214 outflow velocity in a time of 1.6 times the secondary vortex half-life. The factor of 1.6 was  
215 estimated as resulting in the outflow velocity reaching its maximum as the rear of the vortex  
216 passes  $x_m$ , and variation of this factor (not shown) demonstrates that the chosen value gives  
217 the best fit to the experimental data.
- 218 g) The secondary vortex moves horizontally at the same speed as the primary vortex. No relative  
219 motion has been included in this version of the model.

220 Note that these assumptions were only applied for the evaluation of the best fit, and not for  
221 the parametric variation presented in Section 4.2.

222 Configurations for which the peak maximum velocity did not occur at  $x/D = 1.50$  and  
223  $0.01 \leq z/D \leq 0.04$  (as seen in the UoB data), or for which the peak maximum velocity was  
224 more than  $\pm 0.1m/s$  from the experimental value were discarded. For the acceptable  
225 configurations, “Best Fit” was evaluated using the root mean square (RMS) difference between  
226 the UoB experimental data and the model output. The data used for this calculation included the  
227 vertical profiles of local maximum radial velocity at  $x/D = 1.00, 1.25, 1.50$  and  $1.75$ , and also  
228 the velocity time-series at the position of maximum radial velocity. The vertical profile at  
229  $x/D = 2.00$  and  $2.50$  were not used for reasons discussed below. To account for the  $x/D =$   
230  $1.25$  and  $1.75$  profiles containing a limited number of points, the RMS value for the profiles was  
231 scaled by  $1/N_z$ , where  $N_z$  is the number of measured points in the profile. Vertical profile and  
232 time-series RMS values were otherwise weighted equally.

233 The Best Fit values for the model parameters are given in Table 1. Where available, the  
234 estimated parameters from the UoB experiments are also included in this table. It should be  
235 noted, however, that these estimates were made from flow visualisation work which, at the time,  
236 was intended as purely qualitative. Other parameters, such as the relative size of the secondary  
237 vortex and its aspect ratio, are consistent with the numerical simulations of Mason [3].

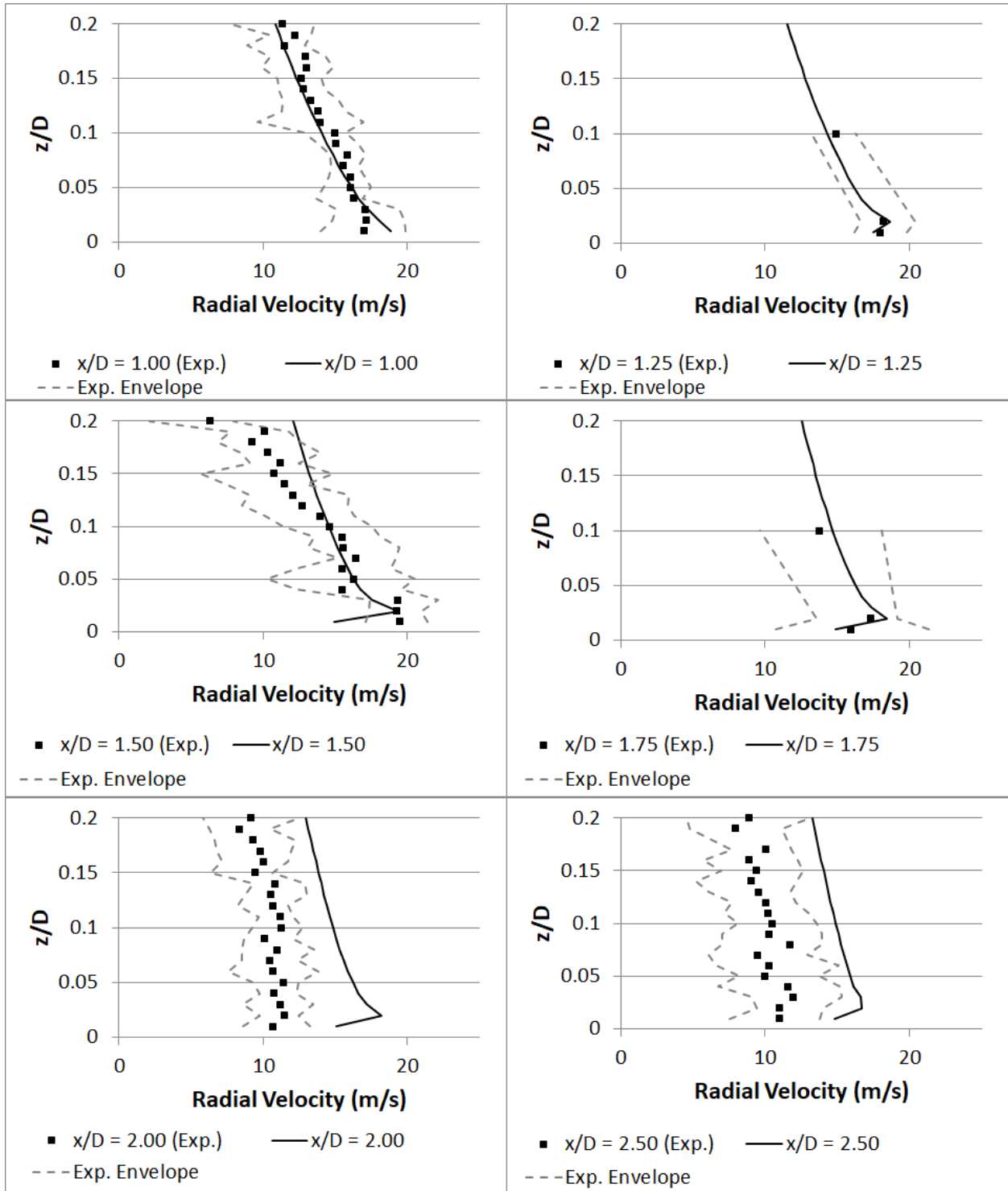


239 4.1 *Best Fit*

240 Using the Best Fit model parameters shown in Table 1, the vertical profiles of radial velocity  
241 have been calculated for the same radial positions as were used for the non-translating UoB-  
242 TWS experiments (Figure 4), and the time-series calculated at the position of global maximum  
243 radial velocity (Figure 5). For  $x/D \leq 1.75$  the experimental data are modelled well by the Best  
244 Fit profiles – with the exception of the  $x/D = 1.50$  profile at  $z/D = 0.01$  data (discussed  
245 below) and isolated points above  $z/D = 0.15$  (equivalent to 800m full-scale), all data fall  
246 within envelope of individual run values. As the secondary vortex strengthens the “nose” of the  
247 typical downburst vertical profile becomes evident. Beyond this position, the vortices decay  
248 rapidly in the physical simulations, a decay not accurately modelled by the vortex model (Figure  
249 4, bottom subplots) for this reason, these vertical sections were not used for the best fit  
250 calculation outlined in Section 3.2). Another difference is in the vertical spread of the “nose”,  
251 which spans the lowest three data points in the UoB-TWS data. The vortex model creates a sharp  
252 nose where the outflow velocities from the two Rankine-type vortices combine; each vortex will  
253 have a clearly defined radius of maximum tangential velocity, resulting in this sharply defined,  
254 high-speed region. It is possible that the interaction of the primary and secondary vortices is  
255 distorting the flow field in this region, making the Rankine-type model inappropriate.  
256 Notwithstanding these differences, the vortex model is shown to give a good representation of  
257 the flow field over the main region of interest, from the edge of the downdraft to the radius of  
258 maximum velocity and slightly beyond.

259 At the point of global maximum radial velocity, the model also captures the main features of  
260 the velocity time-series (Figure 5). The initial acceleration is slightly lower (~5%) in the vortex  
261 model, with a narrower peak (~30%). The deceleration phase from the model also matches the  
262 experimental data, with the final outflow velocity matched. The narrower peak may be due to the  
263 simplifications and assumptions made in the position and motion of the secondary vortex (which  
264 is not modelled as moving up and around the perimeter of the primary vortex, indicated by  
265 Mason et al. ([3])). Incorporation of these more complex relationships may be included in future  
266 model development.

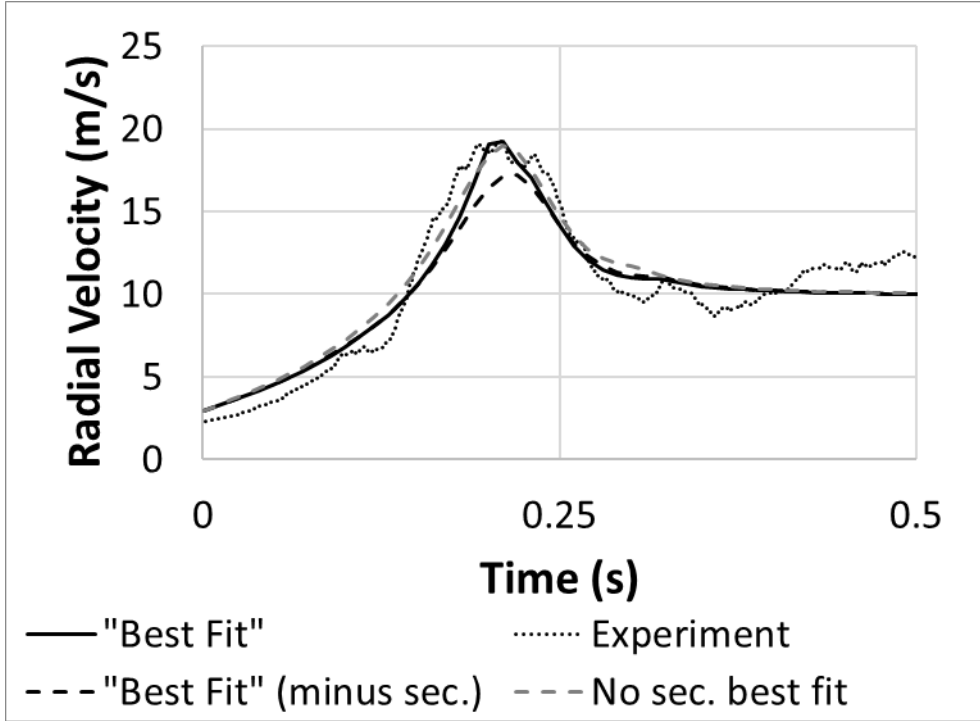
267  
 268  
 269  
 270  
 271  
 272  
 273  
 274  
 275  
 276  
 277  
 278  
 279  
 280  
 281  
 282  
 283  
 284  
 285  
 286  
 287  
 288  
 289  
 290  
 291  
 292  
 293  
 294  
 295  
 296  
 297  
 298  
 299  
 300  
 301



302 **Figure 4: Comparison of vortex model Best Fit output with UoB-TWS experimental data (“Exp.”). The**  
 303 **envelope of the UoB experimental data (“Exp. Envelope”) is the upper and lower bounds of the individual**  
 304 **run velocities at the time of the ensemble maximum.**

305

306  
307  
308  
309  
310  
311  
312  
313  
314  
315  
316  
317  
318  
319  
320  
321  
322  
323



324 **Figure 5: Model and experimental radial velocity time-series at the point of the global maximum velocity in**  
325 **the UoB experiments. “Best Fit” (minus sec.)’ uses the Best Fit parameters except with no secondary vortex.**  
326 **‘No sec. best fit’ is the best fit obtained if there is no secondary vortex and other parameters are varied.**

327 *4.2 Parametric Study*

328 In order to assess the importance of the secondary vortex, the model was run using the  
329 primary vortex parameters from the Best Fit configuration but no secondary vortex. The model  
330 was also run to determine the best fit achievable with no secondary vortex. In the former case,  
331 the maximum radial velocity is approximately 11% lower ( $17.2m/s$  rather than  $19.3m/s$ ), and  
332 the acceleration is reduced (Figure 5). In the latter case, the velocity time-series at  $x/D = 1.50$   
333 is negligibly different from the Best Fit series. However, examination of the vertical distributions  
334 of the radial velocity component (Figure 6 and Figure 4) shows the importance of the secondary  
335 vortex, which is responsible for the development of the profile close to the ground and the  
336 prominent “nose” of the typical downburst profile.

337

338  
 339  
 340  
 341  
 342  
 343  
 344  
 345  
 346  
 347  
 348  
 349  
 350  
 351  
 352  
 353  
 354  
 355  
 356  
 357  
 358  
 359  
 360  
 361  
 362  
 363  
 364  
 365  
 366  
 367  
 368  
 369  
 370  
 371  
 372  
 373  
 374  
 375  
 376  
 377

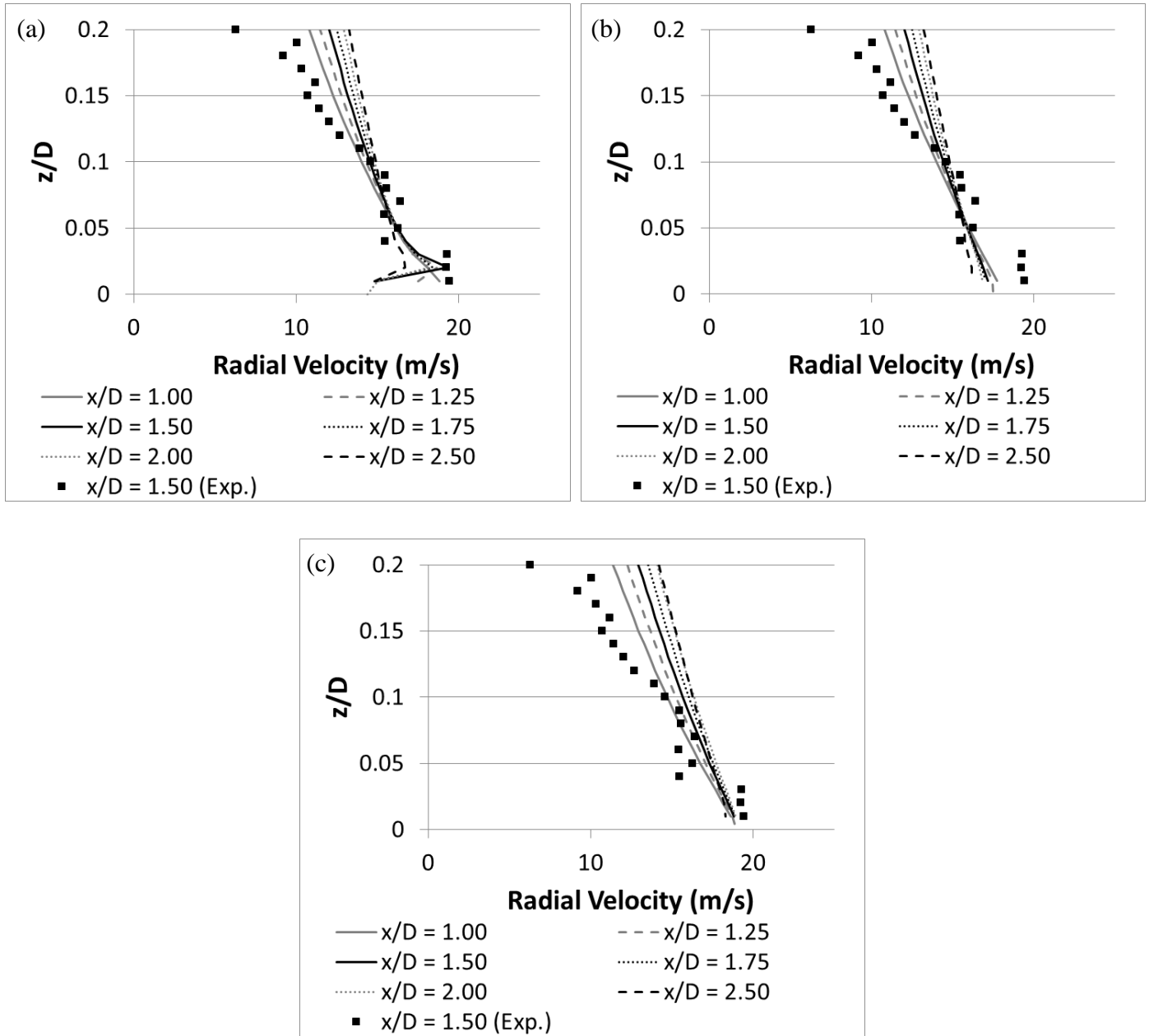
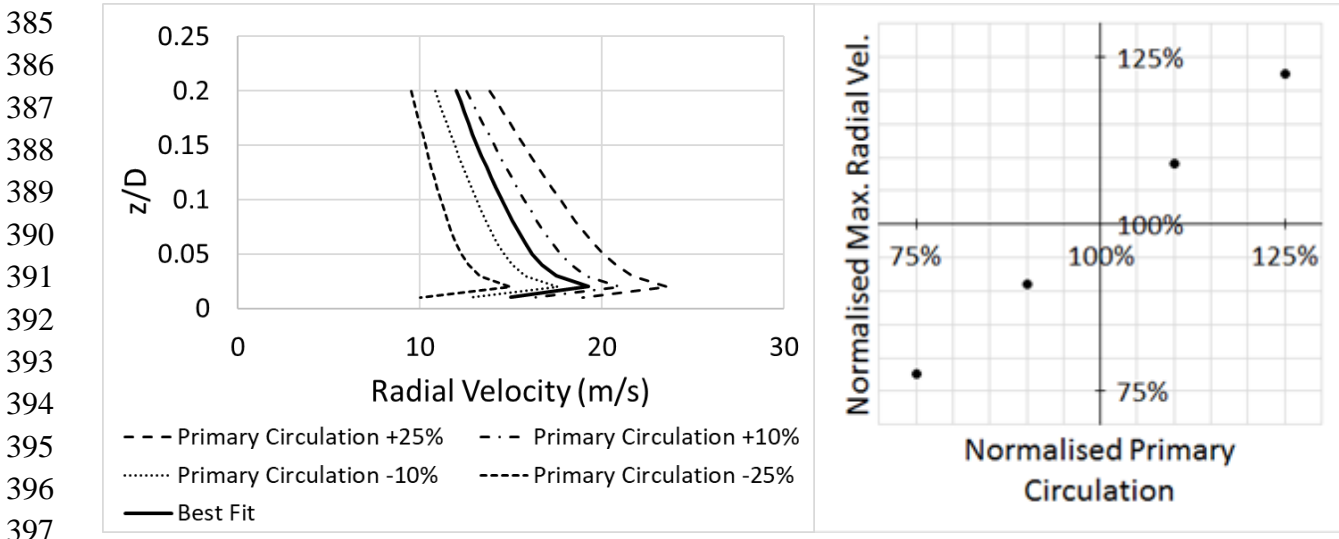


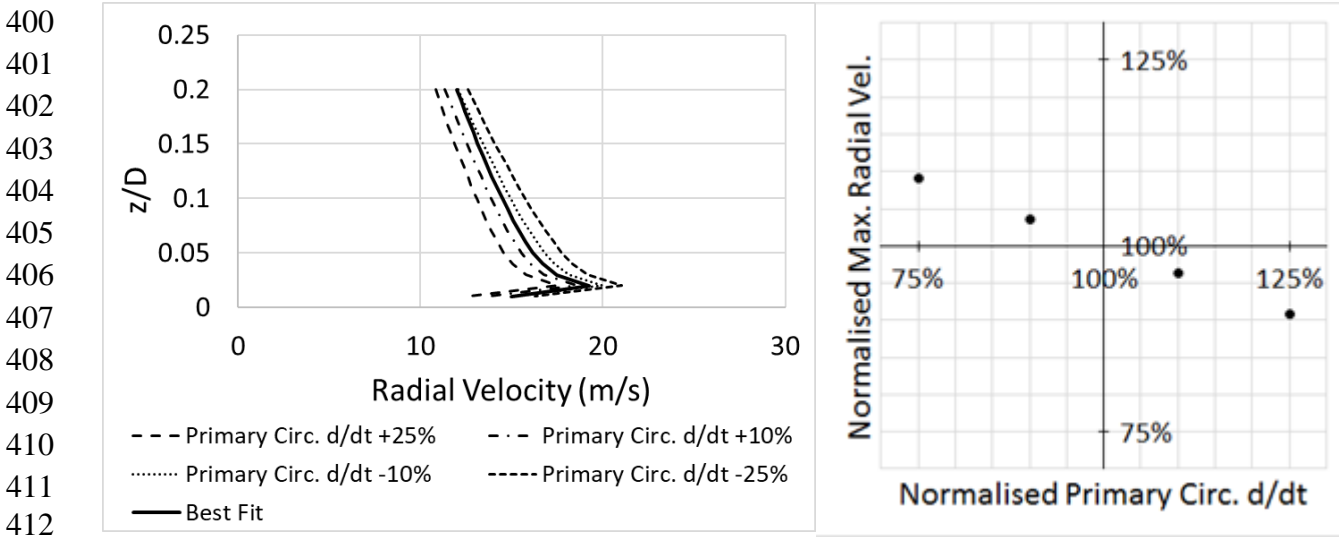
**Figure 6: Vertical distributions of radial velocity for (a) Best Fit configuration, (b) configuration as for Best Fit configuration but with no secondary vortex, and (c) the best fit found if no secondary vortex is permitted.**

Using the Best Fit parameter values as a baseline, each parameter was varied in turn in order to quantify the sensitivity of the model output to that parameter. Variations of -25%, -10%, +10% and +25% of the Best Fit value were used. Only parameters for which the variation had a significant effect on the model output are discussed here. Variation of the primary vortex initial circulation (Figure 7) changes the magnitude the vertical profile of radial velocity while maintaining the same qualitative profile, with the maximum radial velocity varying approximately linearly with the circulation. Changing the initial circulation of the primary vortex

378 does not change the relative positions of the primary and secondary vortices, nor does it change  
 379 the relative rate of change of the two circulations (due to the assumption made in section 3.2),  
 380 thus the position of the peak maximum radial velocity is unchanged by changing the initial  
 381 circulation. The rate of change of primary circulation has a smaller effect (9% change in  $u_m$  for  
 382 a 25% parameter change), and the variation is inversely, linearly proportional (Figure 8). The  
 383 inverse law would be expected due to this rate of change being negative (i.e. a weakening vortex)  
 384 and so a percentage increase accelerates the weakening.



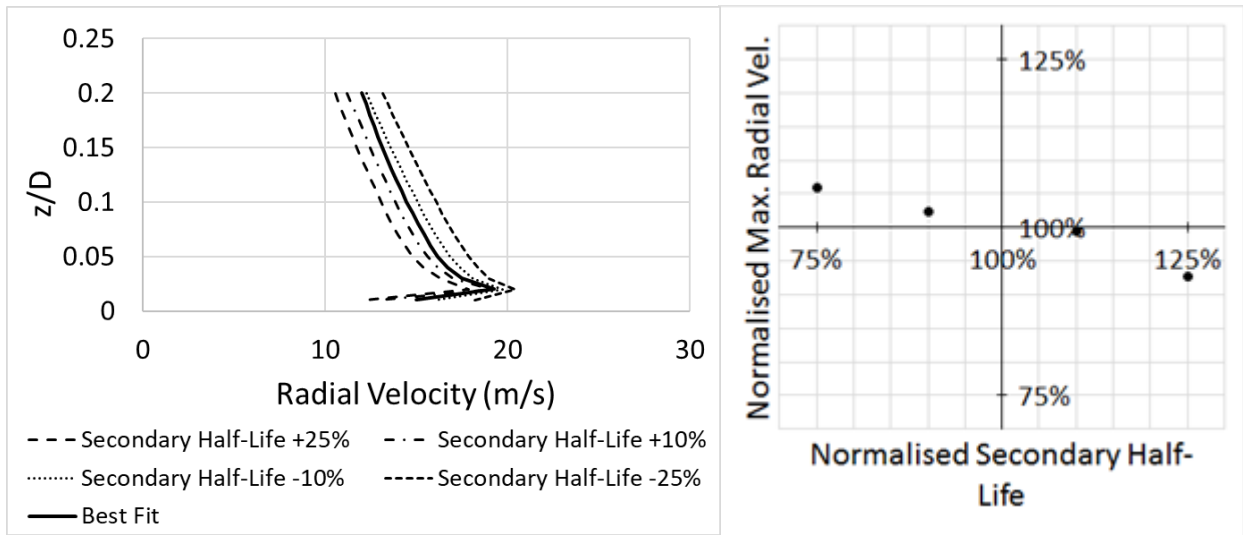
398 **Figure 7: Effect of varying the primary circulation. Vertical profile of radial velocity at  $x/D = 1.50$  and**  
 399 **normalised variation. Normalisation is by the Best Fit value.**



413 **Figure 8: Effect of varying the rate of change ( $d/dt$ ) of the primary circulation. Vertical profile of radial**  
 414 **velocity at  $x/D = 1.50$  and normalised variation. Normalisation is by the Best Fit value.**

415 The initial secondary circulation is zero, as required by the hypothesised method of its  
 416 formation, and so its variation has not been considered. Further, realistically sized variations of  
 417 the rate of change of secondary vortex circulation have negligible effect on  $u_m$  or  $z_m$ . The

418 impact of varying the half-life of the secondary vortex is more complex. With a shorter half-life,  
 419 the secondary vortex reaches its maximum circulation more quickly. Consequently, the primary  
 420 vortex has a greater circulation at this instant, and (with the rate of change of the secondary  
 421 vortex radii being positive) the secondary vortex is smaller than at later times, resulting in a  
 422 higher velocity for the same circulation. This latter point is, arguably, an artefact of the model  
 423 rather than necessarily representative of the physical system. The result of this is an increase in  
 424  $u_m$  as the half-life decreases, and the maximum velocity at  $x/D = 1.50$  occurring earlier  
 425 (Figure 9). This change in  $u_m$  is non-linear due to the complex relationship between  $u_m$  and the  
 426 instantaneous strengths of both vortices – an increase of the same percentage results in a larger  
 427 magnitude change than the corresponding decrease (Figure 9). The time of occurrence, and  
 428 therefore radial location, of  $u_m$  is also dependent on the half-life; for a 25% increase in the half-  
 429 life  $u_m$  occurs at  $x/D = 1.00$ , while for a 25% decrease it remains at  $x/D = 1.50$  (not shown).



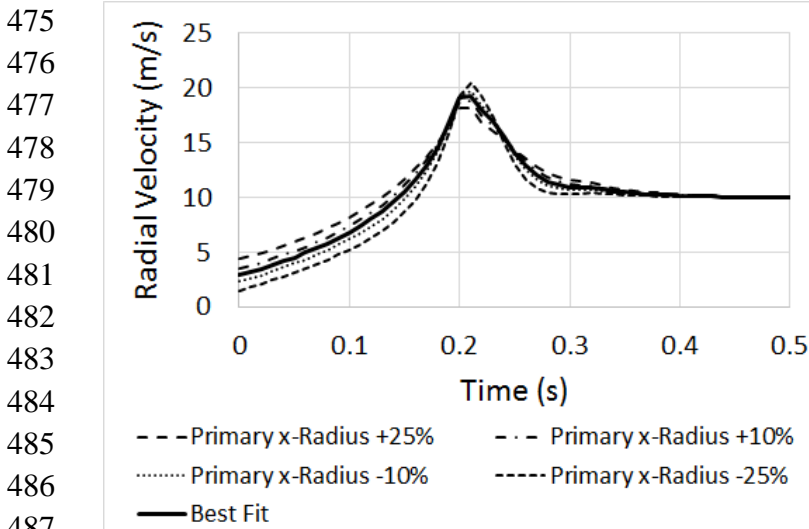
446 **Figure 9: Effect of varying the half-life of the secondary vortex. Radial velocity time-series at  $x/D = 1.50$**   
 447 **and normalised variation. Normalisation is by the Best Fit value.**

448  
 449 Increasing the initial x-radius of the primary vortex increases the width of the time-series peak  
 450 (Figure 10). On first inspection, this may appear to give opportunity to further refine the model  
 451 output, due to the Best Fit peak being narrower than shown in the experimental data (Figure 5).  
 452 However, the broadening of the peak around the time of maximum velocity is limited, and the  
 453 additional size of the vortex also increases the initial velocity at  $x/D = 1.50$ , reducing the  
 454 acceleration phase of the outflow. Due to possible overshoot effects, modelling this acceleration  
 455 phase is arguably more important than widening the peak to match the plateau in the  
 456 experimental data.

457 Moving the starting x-position of the primary vortex (which is, by assumption (Section 3.2),  
 458 with the rear edge of the vortex at the edge of the downdraft region) towards the centre of the  
 459 downdraft is physically unrealistic. Conversely, it is conceivable that the primary vortex will

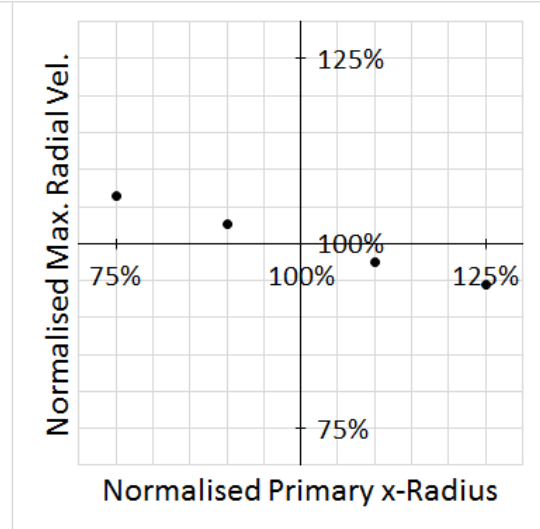
460 start a distance away from the downdraft edge, with the downdraft almost certainly not being a  
 461 perfect circle as is generally assumed. Due to the design of the model, such a variation would  
 462 only have the effect of shifting  $x_m$ , the radial position of  $u_m$ , by an equivalent amount and so  
 463 this will not be discussed further. Of more interest is the starting position of the secondary  
 464 vortex, as this will be determined by the precise mechanism of its formation and, likely, the  
 465 roughness of the ground the downburst forms over. Variation of this parameter shows a decrease  
 466 in the maximum velocity at  $x/D = 1.50$  (Figure 11) for both an increase and decrease.  
 467 Increases show a proportionally larger reduction, though again the changes are small relative to  
 468 those caused by a change in the primary circulation. Further, for increases in the secondary  
 469 starting x-position,  $x_m$  moves towards the downdraft region, with  $u_m$  occurring at  $x/d =$   
 470 1.00 for a 25% increase. Again, due to the interaction of the primary and secondary vortices,  
 471 and their rates of strengthening/decay, there is no clear pattern for the change of  $x_m$ . For a 10%  
 472 decrease in secondary starting x-position  $x_m/D = 1.25$  but for a 25% decrease it reverts to  
 473  $x/D = 1.50$ .

474

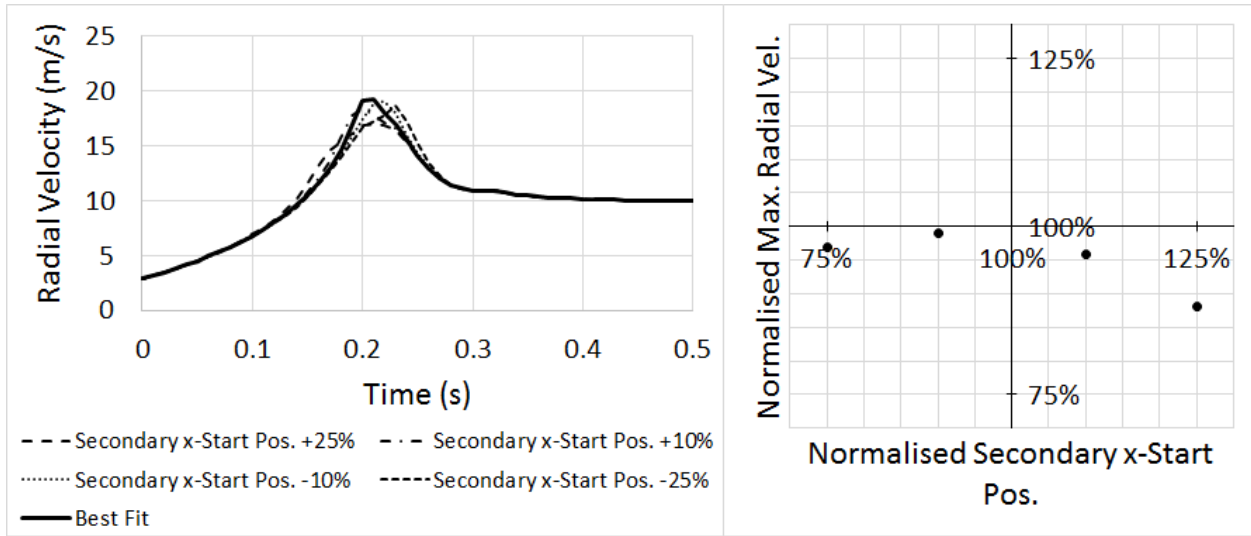


488 **Figure 10: Effect of varying the initial x-radius of the primary vortex. Radial velocity time-series at  $x/D =$**   
 489 **1.50 and normalised variation. Normalisation is by the Best Fit value.**

490



491  
 492  
 493  
 494  
 495  
 496  
 497  
 498  
 499  
 500  
 501  
 502  
 503



504  
 505

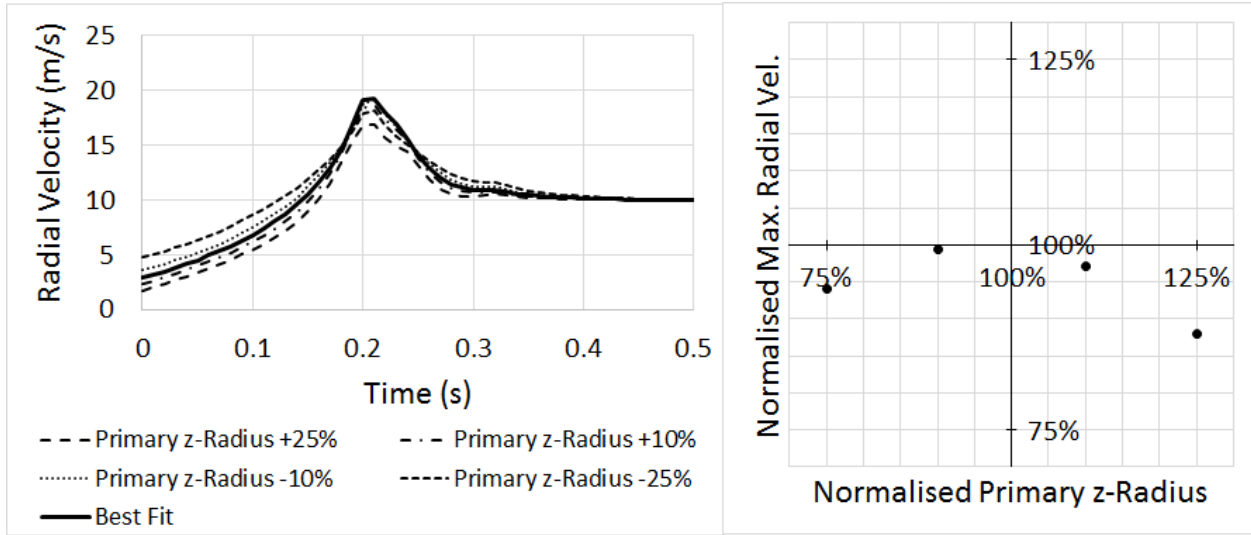
**Figure 11: Effect of varying the initial x-start position of the secondary vortex. Radial velocity time-series at  $x/D = 1.50$  and normalised variation. Normalisation is by the Best Fit value.**

506  
 507  
 508  
 509  
 510  
 511  
 512  
 513  
 514  
 515  
 516

Changing the initial  $z$ -radius of the primary vortex does not change  $x_m$  but does reduce  $u_m$  in a similar manner to that seen for the secondary vortex  $x$ -start position (Figure 12). The base of the time-series peak is also widened as the initial  $z$ -radius decreases, and the initial velocity increases. The change in the initial primary  $z$ -radius causes assumption (e) (Section 3.2) to no longer hold, and the circumferences of the two vortices to no longer meet. This separation causes a change in the vertical profile of radial velocity (Figure 13) which may account for the stepped shape of the profile nose seen in Figure 4 for  $x/D = 1.50$ , where there is a sharp deceleration around  $z/D = 0.06$ . Varying the  $z$  start position of the primary vortex has the same effect, as would be expected given the reasons for the changes.



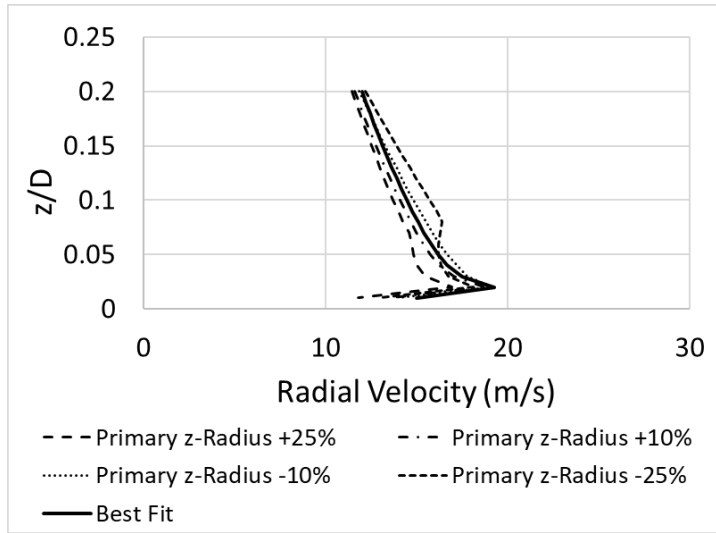
517  
 518  
 519  
 520  
 521  
 522  
 523  
 524  
 525  
 526  
 527  
 528  
 529  
 530



531  
 532

**Figure 12: Effect of varying the initial z-radius of the primary vortex. Radial velocity time-series at  $x/D = 1.50$  and normalised variation. Normalisation is by the Best Fit value.**

533  
 534  
 535  
 536  
 537  
 538  
 539  
 540  
 541  
 542  
 543  
 544  
 545  
 546



547  
 548

**Figure 13: Effect of varying the initial z-radius of the primary vortex. Vertical profile of radial velocity at  $x/D = 1.50$  and normalised variation. Normalisation is by the Best Fit value.**

549 **5 CONCLUSIONS**

550  
 551  
 552  
 553

In this paper, we have outlined a simple, analytical model which is shown to appropriately capture the main features of a thunderstorm downburst outflow. Both the primary and secondary vortices associated with downburst flows are modelled. A parametric analysis shows that the maximum wind speed,  $u_m$ , varies linearly with initial primary circulation, and has an inverse,

554 linear relationship with rate of decay of the primary vortex. The half-life of the secondary vortex,  
555 which forms and then decays once the primary vortex starts to move outwards from the  
556 downdraft impingement point, has a more complex, inverse, non-linear relationship with  $u_m$ ,  
557 and also affects the time at which  $u_m$  occurs; the relationship between the initial position of the  
558 secondary vortex and  $u_m$  is more complex still. The shape of the downburst “nose” is shown to  
559 be dependent on the vertical separation of the primary and secondary vortices, modelled in the  
560 parametric study as a variation of the primary vortex height or vertical starting position.

561 It is acknowledged that a number of simplifying assumptions have been made along the  
562 way. For example:

- 563 • The rates of change of vortex parameters such as dimensions and circulation have  
564 been assumed constant, which leads to discrepancies between the model output and  
565 experimental data during the latter parts of the downburst lifecycle. Given sufficient  
566 data it would be relatively easy to address this issue, although the experiments  
567 themselves would not be straight forward to undertake.
- 568 • The full motion of the secondary vortex relative to the primary vortex is not modelled  
569 (some previous numerical work indicates a lifting of this vortex as it rolls around the  
570 primary); again, this is of more importance later in the vortex development, after the  
571 peak wind speeds have occurred, and is arguably of much lesser engineering  
572 importance if, for example, it is only the wind induced forces on a structure that are of  
573 concern.
- 574 • The near ground behaviour (heights <10m) is not accurately described by the model  
575 due to its inviscid nature. However, to the authors’ knowledge there are currently no  
576 data available for the boundary layer development of downburst flow in this region.  
577 As such data become available a model to describe the flow in this region could easily  
578 be incorporated as a separate flow regime, where ground effects dominate the vortex  
579 flow field.
- 580 • Further validation of the full flow field and the spatio-temporal variation of circulation  
581 and vortex structure is required. To this point the model has been validated against a  
582 single (albeit advanced) physical simulation of a transient, non-translating downburst.  
583 While further validation against other simulation data sets is possible, the physical  
584 simulations used for the validation are known to be consistent with the available data  
585 from other simulations. Of potentially more value will be future validation against  
586 detailed full-scale downburst data of the type currently being gathered at other  
587 institutions.

588 Notwithstanding the above simplifications, the results are rather remarkable and offer, for the  
589 first time, a computationally inexpensive tool which could be incorporated into a framework of  
590 the type proposed by [23], thereby informing the design process.

592 The authors would like to thank the UK Engineering and Physical Science Research Council,  
 593 which funded the original research on which this model is based under grant number  
 594 EP/J008281/1.

## 595 7 REFERENCES

- 596 [1] T. T. Fujita, ‘Downburst: Microburst and macroburst’, *Univ. Chic. Press IL*, p. pp.-p. 122,  
 597 1985.
- 598 [2] J. Kim and H. Hangan, ‘Numerical simulations of impinging jets with application to  
 599 downbursts’, *J. Wind Eng. Ind. Aerodyn.*, vol. 95, pp. 279–298, 2007.
- 600 [3] M. S. Mason, G. S. Wood, and D. F. Fletcher, ‘Numerical simulation of downburst winds’,  
 601 *J. Wind Eng. Ind. Aerodyn.*, vol. 97, pp. 523–539, 2009.
- 602 [4] E. C. C. Choi, ‘Field measurement and experimental study of wind speed profile during  
 603 thunderstorms’, *J. Wind Eng. Ind. Aerodyn.*, vol. 92, pp. 275–290, 2004.
- 604 [5] F. T. Lombardo, ‘Thunderstorm characteristics of wind engineering importance’, presented  
 605 at the In Proceedings of the 13th International Conference on Wind Engineering, 2011.
- 606 [6] F. T. Lombardo, D. A. Smith, J. L. Schroeder, and K. C. Mehta, ‘Thunderstorm  
 607 characteristics of importance to wind engineering’, *J. Wind Eng. Ind. Aerodyn.*, vol. 125,  
 608 pp. 121–132, 2014.
- 609 [7] H. E. Brooks, ‘Severe thunderstorms and climate change’, *Atmospheric Res.*, vol. 123, no.  
 610 0, pp. 129–138, 2013.
- 611 [8] K. Butler and A. Kareem, ‘Physical and numerical modeling of downburst generated gust  
 612 fronts’, presented at the Proceedings of the 12th International Conference on Wind  
 613 Engineering, Cairns, Australia, 2007, pp. 791–798.
- 614 [9] M. T. Chay and C. W. Letchford, ‘Pressure distributions on a cube in a simulated  
 615 thunderstorm downburst - Part A: stationary downburst observations’, *J. Wind Eng. Ind.  
 616 Aerodyn.*, vol. 90, no. 7, pp. 711–732, 2002.
- 617 [10] M. T. Chay and C. W. Letchford, ‘Pressure distributions on a cube in a simulated  
 618 thunderstorm downburst - Part B: moving downburst observations’, *J. Wind Eng. Ind.  
 619 Aerodyn.*, vol. 90, no. 7, pp. 733–753, 2002.
- 620 [11] M. Jesson, M. Sterling, C. Letchford, and C. Baker, ‘Aerodynamic forces on the roofs of  
 621 low-, mid- and high-rise buildings subject to transient winds’, *J. Wind Eng. Ind. Aerodyn.*,  
 622 vol. 143, pp. 42–49, 2015.
- 623 [12] M. Jesson, M. Sterling, C. Letchford, and M. Haines, ‘Aerodynamic forces on generic  
 624 buildings subject to transient, downburst-type winds’, *J. Wind Eng. Ind. Aerodyn.*, vol. 137,  
 625 pp. 58–68, 2015.
- 626 [13] T. S. Lundgren, J. Yao, and N. N. Masour, ‘Microburst modelling and scaling’, *J. Fluid  
 627 Mech.*, vol. 239, pp. 461–488, 1992.
- 628 [14] L. G. Orf, C. Oreskovic, E. Savory, and E. Kantor, ‘Circumferential analysis of a simulated  
 629 three-dimensional downburst-producing thunderstorm outflow’, *J. Wind Eng. Ind.  
 630 Aerodyn.*, vol. 135, pp. 182–190, 2014.
- 631 [15] B. C. Vermeire, L. G. Orf, and E. Savory, ‘Improved modelling of downburst outflows for  
 632 wind engineering applications using a cooling source approach’, *J. Wind Eng. Ind.  
 633 Aerodyn.*, vol. 99, no. 8, pp. 801–814, 2011.
- 634 [16] A. C. McConville, M. Sterling, and C. J. Baker, ‘The physical simulation of thunderstorm  
 635 downbursts using an impinging jet’, *Wind Struct.*, vol. 12, no. 2, pp. 133–149, 2009.
- 636 [17] J. D. Holmes and S. E. Oliver, ‘An empirical model of a downburst’, *Eng. Struct.*, vol. 22,  
 637 pp. 1167–1172, 2000.

- 638 [18] M. Ivan, ‘A ring-vortex downburst model for flight simulations’, *J. Aircr.*, vol. 23, no. 3,  
639 pp. 232–236, 1986.
- 640 [19] T. A. Schultz, ‘Multiple vortex ring model of the DFW microburst’, *J. Aircr.*, vol. 27, no. 2,  
641 pp. 163–168, 1990.
- 642 [20] M. R. Hjelmfelt, ‘Structure and life cycle of microburst outflows observed in Colorado’, *J.*  
643 *Appl. Meteorol.*, vol. 27, no. August, pp. 900–927, 1988.
- 644 [21] M. Jesson and M. Sterling, ‘A simple vortex model of a thunderstorm downburst’,  
645 presented at the 12th UK Conference on Wind Engineering, Nottingham, UK, 2016.
- 646 [22] M. R. Haines, ‘The simulation of non-synoptic effects and their implications for  
647 engineering structures’, University of Birmingham, UK, Birmingham, 2015.
- 648 [23] C. J. Baker and M. Sterling, ‘A conceptual model for wind and debris impact loading of  
649 structures due to tornadoes’, *J. Wind Eng. Ind. Aerodyn.*, In Press.
- 650
- 651